CHEMISTRY

[NiFe], [FeFe], and [Fe] hydrogenase models from isomers

Seiji Ogo[1,2,3]*, Takahiro Kishima[1,2], Takeshi Yatabe[1,2,3], Keishi Miyazawa[1,2], Ryunosuke Yamasaki[1,2], Takahiro Matsumoto[1,2,3], Tatsuya Ando[1,2,3], Mitsuhiro Kikkawa[1,2,3], Miho Isegawa[3], Ki-Seok Yoon[2,3], Shinya Hayami[4]

The study of hydrogenase enzymes (H_2ases) is necessary because of their importance to a future hydrogen energy economy. These enzymes come in three distinct classes: [NiFe] H_2ases, which have a propensity toward H_2 oxidation; [FeFe] H_2ases, which have a propensity toward H_2 evolution; and [Fe] H_2ases, which catalyze H^- transfer. Modeling these enzymes has so far treated them as different species, which is understandable given the different cores and ligand sets of the natural molecules. Here, we demonstrate, using x-ray analysis and nuclear magnetic resonance, infrared, Mössbauer spectroscopies, and electrochemical measurement, that the catalytic properties of all three enzymes can be mimicked with only three isomers of the same NiFe complex.

INTRODUCTION

A hydrogen energy economy will require not only catalysts capable of H_2 oxidation but also those that can put it back together again. The design of these catalysts takes much inspiration from hydrogenase enzymes (H_2ases) because they perform just such chemistry in nature (1–4). These enzymes come in three distinct varieties, as determined by the metals at their active sites: [NiFe] H_2ases, [FeFe] H_2ases, and [Fe] H_2ases (Fig. 1) (5–7). The H_2ases can be classified according to their reactivity differences, as well as their structural differences. [NiFe] H_2ases are more useful for H_2 oxidation than evolution, while [FeFe] H_2ases are more useful for H_2 evolution, and [Fe] H_2ases can catalyze hydride (H^-) transfer (5). It is not surprising then that model studies have so far treated these three H_2ases as different species.

[NiFe] H_2ases have been of particular interest to us, owing to their potential application in fuel cells, and so we have produced a series of model compounds that successfully mimic H_2ase chemical and catalytic behavior (8, 9). This series culminated in the production of a NiFe complex that is capable of performing electron (e^-) and H^- transfer from H_2 and H_2 evolution. This complex, $[Ni^{II}(Z)Fe^{II}(MeCN)\{P(OEt)_3\}_3](BPh_4)_2$ (Z = N,N'-diethyl-3,7-diazanonane-1,9-dithiolato, and Me, Et, and Ph indicate methyl, ethyl, and phenyl groups, respectively), is based on a central NiFe bimetallic core; flexible μ-S bridges, which allow close approach of the two metal centers; a labile monodentate ligand (MeCN), which acts as a vacant site; and three $P(OEt)_3$ ligands, which can accept π-back donation from Fe (8). Despite its successes, however, this complex was only able to perform single turnover, meaning we still had some way to go.

Examining the three classes of H_2ases more closely, we noticed the following relationships between the Fe ligands: In [NiFe] H_2ase, the possible H_2 active site (X in Fig. 1) is between the Fe and Ni centers and trans to a CO ligand; in [FeFe] H_2ase, the possible H_2 active site is both trans and cis to two CO ligands; and in [Fe] H_2ase, the possible H_2 active site is cis to two CO ligands (5). It therefore occurred to us that creating this series of isomers of a [NiFe] H_2ase model complex might provide important insights into the differing reactivity of the H_2ases.

We settled on the following arrangement. First, the flexible μ-S bridges and Ni environment remain. Second, the Fe labile ligand was changed from MeCN to Cl^- because it is not only labile but also a weak Lewis base, meaning it is able to remove the proton generated during the reaction cycle. Last, to fix the coordination geometry as far as possible and maintain π-back donation, we settled on 1,2-bis(diphenylphosphino)ethane (L) and the CO ligand that determines, based on its relationship to the possible H_2 active site, the principle reactivity of the complex.

Here, we report that the different isomers of a [NiFe] H_2ase model complex have the expected relationship in reactivity and their crystal structures. Furthermore, we report catalytic e^- transfer,
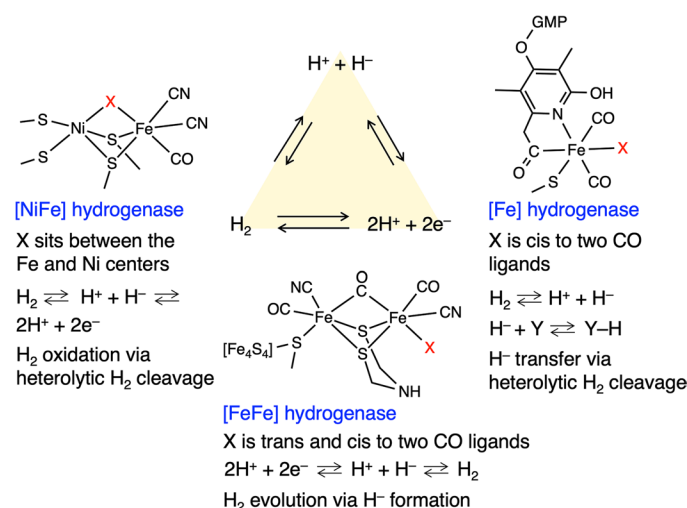
Fig. 1. The active site structures of [NiFe] H_2ases that mainly catalyze H_2 oxidation reactions, [FeFe] H_2ases that mainly catalyze H_2 evolution reactions, and [Fe] H_2ases that catalyze H^- transfer to the substrate via heterolytic H_2 cleavage. X, possible H_2 active sites; Y, methenyltetrahydromethanopterin; GMP, guanosine monophosphate.

[1]Department of Chemistry and Biochemistry, Graduate School of Engineering, Kyushu University, 744 Moto-oka, Nishi-ku, Fukuoka 819-0395, Japan. [2]Center for Small Molecule Energy, Kyushu University, 744 Moto-oka, Nishi-ku, Fukuoka 819-0395, Japan. [3]International Institute for Carbon-Neutral Energy Research (WPI-I²CNER), Kyushu University, 744 Moto-oka, Nishi-ku, Fukuoka 819-0395, Japan. [4]Graduate School of Science and Technology, Kumamoto University, 2-39-1 Kurokami, Chuo-ku, Kumamoto 860-8555, Japan.
*Corresponding author. Email: ogo.seiji.872@m.kyushu-u.ac.jp

H_2 evolution, and H^- transfer in water using the [NiFe] H_2ase model complex.

RESULTS AND DISCUSSION

Synthesis and structures of hydride isomers

Water-soluble $Ni^{II}Fe^{II}$ complex $[Ni^{II}(Z)Fe^{II}(Cl)(CO)(L)](Cl)$ {[1] (Cl)} was prepared from the reaction of $[Ni^{II}(Z)]$ with $[Fe^{II}(L)(Cl)_2]$ under a CO atmosphere and characterized by x-ray analysis (fig. S1); electrospray ionization–mass spectrometry (ESI-MS; fig. S2); proton nuclear magnetic resonance (^1H NMR; fig. S3), ^{57}Fe Mössbauer (fig. S4), infrared (IR; fig. S5), and electron spin resonance (ESR) spectroscopies; and elemental analysis. The Fe^{II} center is surrounded by L and CO as supporting ligands and Cl^- as a labile ligand.

An Oak Ridge thermal ellipsoid plot (ORTEP) drawing of 1 shows its framework based around the $Ni(\mu$-S$)_2$Fe butterfly core, in which Ni and Fe atoms are tethered by the thiolato units of Z (fig. S1). The distance of Ni···Fe is 3.2685 Å (5), and the angles of Ni—S—Fe are 94.00(2)° and 92.92(2)°. Its structural parameters match well with those optimized by density functional theory (DFT) calculations (fig. S6 and tables S1 to S3). The Ni atom of 1 adopts a square planar geometry with the ligand Z, whereas the Fe atom of 1 adopts a distorted octahedral coordination, where it is surrounded by one CO, one Cl, one bidentate ligand L, and one $[Ni^{II}(Z)]$. The $Ni^{II}Fe^{II}$ complex 1 is diamagnetic, which is evidenced by the appearance of ^1H NMR signals in the diamagnetic region (fig. S3) and the ESR silence at 128 K. The ^{57}Fe Mössbauer spectrum of 1 in the absence of a magnetic field shows an isomer shift of 0.12 mm s^{-1} and a quadrupole doublet of 0.46 mm s^{-1} (fig. S4), which is comparable to the low-spin Fe^{II} center in the $P(OEt)_3$ ligands complex (10). The isomer shift of 1 is well reproduced by the DFT calculation at the meta-generalized gradient approximation (meta-GGA) level (table S4), which supports our assignment of the spin state and the oxidation state of 1.

Complex 1 reacted with H_2 (0.1 to 0.8 MPa) at room temperature in water to give three hydride isomers (Fig. 2): $[Ni^{II}(Z)(\mu$-H)$Fe^{II}(CO)(L)](Cl)$ {[2a](Cl)}, $[Ni^{II}(Z)Fe^{II}(CO)(L)(H)](Cl)$ {[2b](Cl)}, and $[Ni^{II}(Z)Fe^{II}(CO)(L)(H)](Cl)$ {[2c](Cl)}. The reaction was followed by ^1H NMR spectroscopy (fig. S7) and ESI-MS (fig. S8). The ^1H NMR spectrum shows three hydride signals in the metal hydride region, which indicates formation of three structurally different hydride species (fig. S7). The three types of $Ni^{II}Fe^{II}$ hydride complexes were characterized by x-ray analysis (Fig. 3) as well as ^1H NMR (figs. S9 to S11), IR (figs. S12 to S14), ^{57}Fe Mössbauer (figs. S15 to S17), and ESR spectroscopies. The hydride complexes 2a–2c are diamagnetic, as evidenced by the appearance of its ^1H NMR spectrum and the ESR silence at 128 K. The singlet spin states of 2a–2c are expected by the DFT calculations (table S2), in which the DFT-optimized structures (tables S5 to S7) match well with the x-ray structures (tables S8 to S10).

The conditions for crystallization of 2a, 2b, and 2c were optimized by changing solvent, temperature, and counter anion, resulting in the successful isolation of the three $Ni^{II}Fe^{II}$ hydride complexes (fig. S18). The isolation of 2a was performed by crystallization at room temperature (fig. S18, red part), while 2b and 2c were isolated by crystallization at −30°C to prevent their isomerizations (fig. S18, blue and green parts). The ORTEP drawings reveal one bridging hydride species, 2a, and two terminal hydride species, 2b and 2c (Fig. 3). The position of the hydride ligand of 2b is trans to the CO
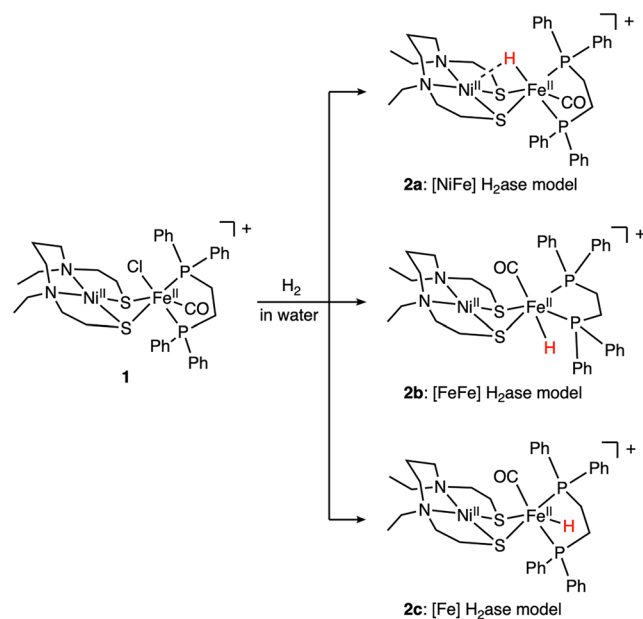
Fig. 2. Formation of three isomers of the hydride complexes, 2a, 2b, and 2c, by the reaction of 1 with H_2 in water.

ligand, analogous to its position in [FeFe] H_2ase. The hydride ligand of 2c is cis to the CO ligand, analogous to its position in [Fe] H_2ase. The Fe—H bond distance [1.47(2) Å] of 2a is much smaller than the Ni—H bond distance [2.04(2) Å], suggesting that the hydride ligand is located on the Fe center (Fig. 3A), analogous to its positions in [NiFe] H_2ase (11). This structural conformation is similar to the previous $Ni^{II}Fe^{II}$ hydride complex [Fe–D: 1.577(17) Å, Ni–D: 2.18(4) Å determined by neutron scattering analysis] (8) but is different to our $Ni^{II}Ru^{II}$ hydride complex [Ru–D: 1.676(8) Å, Ni–D: 1.859(7) Å determined by neutron scattering analysis] (9). The Ni···Fe distance [2.6877(4) Å] of 2a is shorter than those in 2b [3.0534(6) Å; Fig. 3B] and 2c [2.8466(7) Å; Fig. 3C], probably due to the hydride ligand weakly interacting with the Ni atom. This shortened Ni···Fe distance of 2a is related to the Ni—S—Fe angles [72.006(18)° and 72.969(17)°] being shorter in 2a than in 2b [85.68(3)° and 85.70(3)°] and 2c [78.05(3)° and 77.09(3)°]. The Ni···Fe distance [2.6877(4) Å] of 2a is similar to those in the previous $Ni^{II}Fe^{II}$ complex [2.7930(6) Å] and the $Ni^{II}Ru^{II}$ complex [2.739(3) Å]. The Ni—S—Fe angles [72.006(18)° and 72.969(17)°] of 2a are also similar to those of our previous $Ni^{II}Fe^{II}$ complex [75.76(3)° and 75.82(3)°] and the $Ni^{II}Ru^{II}$ complex [70.4(2)° and 70.7(3)°].

The spectroscopic and electrochemical properties of 2a, 2b, and 2c (Table 1) were obtained in organic solvents because the ion pair with PF_6^- or BAr_4^-, necessary for isolation, was insoluble in water. The ^1H NMR spectra of the isolated 2a, 2b, and 2c (figs. S9 to S11) show that the hydride ligands are observed at −2.76 parts per million (ppm) for 2a as a double doublet resonance (fig. S9), −3.83 ppm for 2b as a triplet resonance (fig. S10), and −16.62 ppm for 2c as a double doublet resonance (fig. S11), respectively. The patterns are derived from the hydride ligand coupling with the nuclear spin of two P atoms. The results indicate that the hydride ligand of 2c is the most hydridic (i.e., has the highest electron density) and that of 2a is the least hydridic.
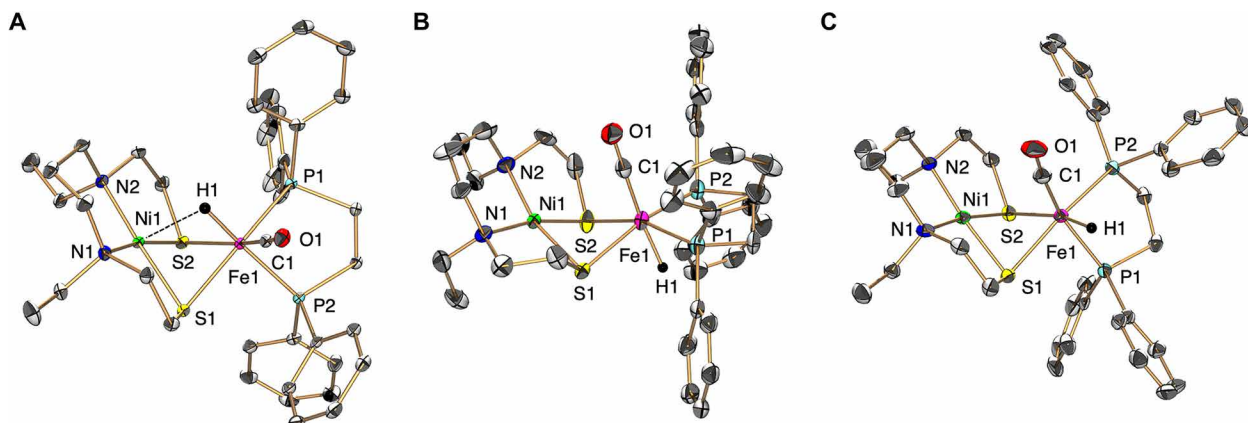
Fig. 3. ORTEP drawings of the solid-state structures of [2a](PF₆), [2b](BAr₄), and [2c](PF₆) with ellipsoids at the 50% probability levels. (**A**) An ORTEP drawing of [**2a**](PF$_6$). H sits between the Fe and Ni centers. The hydrogen atoms (except for the hydride ligand), solvents, and counter anion (PF$_6^-$) are omitted for clarity. Selected interatomic distances (*l*/Å) and angles (φ/deg): Ni1—H1, 2.04(2); Fe1—H1, 1.47(2); Ni1⋯Fe1, 2.6877(4); Fe1—P1, 2.1757(6); Fe1—P2, 2.2562(6); Fe1—S1, 2.3413(5); Fe1—S2, 2.3680(6); Fe1—C1, 1.739(2); Ni1—S1, 2.1731(5); Ni1—S2, 2.1983(6); Ni1—N1, 1.9973(18); Ni1—N2, 1.9864(18); C1—O1, 1.156(3); Ni1—S1—Fe1, 72.969(17); Ni1—S2—Fe1, 72.006(18). (**B**) An ORTEP drawing of [**2b**](BAr₄). H is trans to the CO ligand. The hydrogen atoms (except for the hydride ligand), solvents, and counter anion (BAr₄⁻) are omitted for clarity. BAr$_4^-$: tetrakis(m-terphenyl-5′-yl)borate. Selected interatomic distances (*l*/Å) and angles (φ/deg): Fe1—H1, 1.57(3); Ni1⋯Fe1, 3.0534(6); Fe1—P1, 2.1935(8); Fe1—P2, 2.1772(8); Fe1—S1, 2.3318(8); Fe1—S2, 2.3105(8); Fe1—C1, 1.777(3); Ni1—S1, 2.1544(7); Ni1—S2, 2.1767(7); Ni1—N1, 1.985(2); Ni1—N2, 1.998(2); C1—O1, 1.161(4); Ni1—S1—Fe1, 85.68(3); Ni1—S2—Fe1, 85.70(3). (**C**) An ORTEP drawing of [**2c**](PF$_6$). H is cis to the CO ligand. The hydrogen atoms (except for the hydride ligand) and counter anion (PF$_6^-$) are omitted for clarity. Selected interatomic distances (*l*/Å) and angles (φ/deg): Fe1—H1, 1.42(4); Ni1⋯Fe1, 2.8466(7); Fe1—P1, 2.2448(11); Fe1—P2, 2.1833(11); Fe1—S1, 2.3425(11); Fe1—S2, 2.3771(11); Fe1—C1, 1.744(4); Ni1—S1, 2.1737(10); Ni1—S2, 2.1848(10); Ni1—N1, 1.991(3); Ni1—N2, 1.986(3); C1—O1, 1.167(5); Ni1—S1—Fe1, 78.05(3); Ni1—S2—Fe1, 77.09(3).

Table 1. Spectroscopic properties of 2a, 2b, and 2c and yields of e⁻ transfer, H₂ evolution, and H⁻ transfer reactions of 2a, 2b, and 2c with [Fe^{III}(C₅Me₅)₂]⁺ as an e⁻ acceptor, aqueous acetic acid solution as a H⁺ source, and methylene blue ([MB]⁺) as a H⁻ acceptor. The yields were calculated on the basis of the hydride complexes **2a**, **2b**, and **2c**.

		2a	2b	2c
¹H NMR (ppm)*		−2.76	−3.83	−16.62
IR (cm⁻¹)	ν(C≡O)	1918	1910	1885
	ν(Ni—H—Fe)	1675	–	–
	δ(H—Fe—CO)	–	543	–
	ν(Fe—H)	–	–	1964
Mössbauer	Isomer shift	0.00	0.08	0.14
(mm s⁻¹)	Quadrupole doublet	1.34	1.48	1.13
e⁻ transfer†		57%	27%	33%
H₂ evolution‡		16%	55%	9%
H⁻ transfer§		4%	14%	31%

*The chemical shifts of hydride ligands.   †At room temperature for 1 min.   ‡At room temperature for 30 min.   §At room temperature for 60 min.

The IR spectrum of **2a** shows an isotope-sensitive band at 1675 cm⁻¹, assigned as ν(Ni—H—Fe), which shifted to 1212 cm⁻¹ by using D-labeled **2a** (fig. S12). A similar IR feature was observed for the previous Ni^{II}Fe^{II} complex [ν(Ni—H—Fe) = 1687 cm⁻¹] (*8*). The isotope-sensitive IR band at 543 cm⁻¹ for **2b** shifts to 531 cm⁻¹ by replacement of the H ligand with D and can be assigned as δ(H—Fe—CO) (fig. S13) (*12*). The terminal ν(Fe—H) for **2c** is observed at 1964 cm⁻¹, which shifts to 1414 cm⁻¹ by using D-labeled **2c** (fig. S14) (*13*).

The ^{57}Fe Mössbauer spectra of **2a**–**2c** in the absence of a magnetic field show isomer shifts of 0.00 to 0.14 mm s⁻¹ and quadrupole doublets of 1.13 to 1.48 mm s⁻¹ (figs. S15 to S17), which are similar to the previous Ni^{II}Fe^{II} hydride complex (*10*). These parameters correspond to a low-spin Fe^{II} center with a singlet spin state (*S* = 0). These assignments can be confirmed by DFT calculations at meta-GGA level (tables S2 and S4). The isomer shifts suggest that the Fe center of **2c** has the highest electron density of the three isomers, while that of **2a** has the lowest electron density.

The electrochemical properties of **2a**, **2b**, and **2c** were investigated by cyclic voltammetry in acetonitrile (fig. S19). The redox potentials ($E_{1/2}$) of Fe^{II}/Fe^{I} are observed at −2.040, −2.044, and −2.063 V versus Fc^{+}/Fc (ferrocenium/ferrocene) for **2a**, **2b**, and **2c**, respectively. These results suggest that the geometry of the **2c** ligand set results in the highest electron-donating ability, while that of **2a** has the least electron-donating ability.

The positive-ion ESI mass spectra of **2a**, **2b**, and **2c** all show prominent signals at mass-to-charge ratio (m/z) 789.1, 789.2, and 789.1, which correspond to $[\mathbf{2a}]^{+}$, $[\mathbf{2b}]^{+}$, and $[\mathbf{2c}]^{+}$, respectively. The spectra also showed characteristic isotopic distributions that match well with the calculated isotopic distributions (figs. S20 to S22). To establish the origins of the hydride ligands of **2a**–**2c**, we synthesized D-labeled **2a**–**2c** by using D_2. The mass spectra show the signals at m/z 790.3, 790.3, and 790.2, demonstrating that the original hydride ligands are derived from H_2.

The process of isomerization of the hydride complexes was observed by ^1H NMR spectroscopy (figs. S23 to S25). The results indicate that **2b** is the most thermally unstable, **2a** is the most thermally stable, and **2c** is metastable. The kinetic analysis of isomerization of three hydride complexes was conducted, which indicates that the conversion of **2c** to **2a** ($k_3 = 1.1 \times 10^{-4}$ s^{-1}) is the fastest, and the conversion of **2b** to **2a** ($k_{-1} = 5.0 \times 10^{-5}$ s^{-1}) is faster than that of **2b** to **2c** ($k_2 = 1.5 \times 10^{-5}$ s^{-1}) in acetone (fig. S23). The order of thermodynamic stability agrees with the DFT prediction (table S11).

Reactivity of hydride isomers

The three isomers were compared for reactivity in terms of yield over a given time period (Figs. 4 and 5, figs. S26 to S32, and Table 1). Specifically, e⁻ transfer, H_2 evolution, and H⁻ transfer reactions of the isolated hydride complexes **2a**, **2b**, and **2c** were performed in organic solvents for 1, 30, and 60 min using decamethylferrocenium ion ($[Fe^{III}(C_5Me_5)_2]^{+}$) as the e⁻ acceptor, aqueous acetic acid solution as the H⁺ source, and methylene blue ($[MB]^{+}$) as the H⁻ acceptor, respectively, which were monitored with ultraviolet-visible (UV-vis) absorption spectroscopy and gas chromatography (GC). These results indicate not only that the position of the hydride ligand generates selective reactivity but also that the relative reactivity
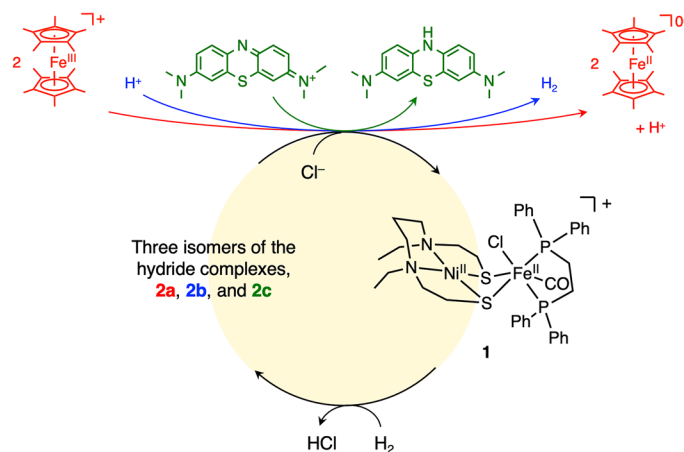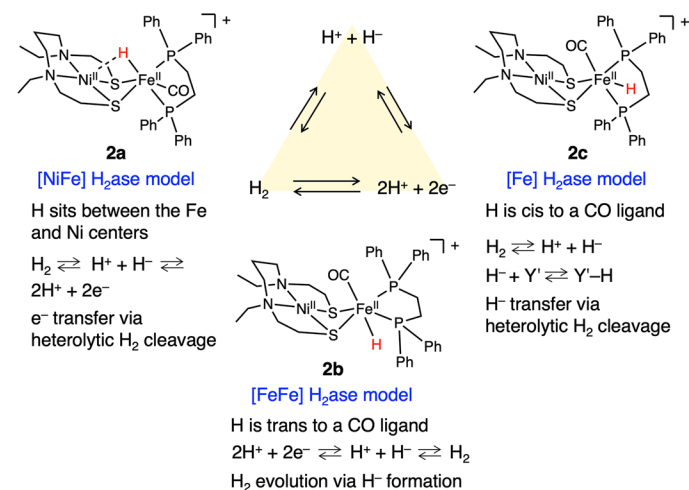
mimics the relative efficiencies of their natural counterparts, i.e., **2a** is the most efficient isomer for e⁻ transfer, as for [NiFe] H_2ase; **2b** is the most efficient isomer for H_2 evolution, as for [FeFe] H_2ase; and **2c** is the most efficient isomer for H⁻ transfer, as for [Fe] H_2ase.

The catalytic reaction of **1**, free to convert between isomers, with H_2 was studied in water. Control experiments, without **1** or H_2, demonstrated that no reaction occurred in their absence. For the e⁻ transfer, $[Fe^{III}(C_5Me_5)_2]^{+}$ was catalytically reduced to decamethylferrocene ($[Fe^{II}(C_5Me_5)_2]$) by H_2 (0.1 to 0.8 MPa), in the presence of catalytic amounts of **1**, at 50°C for 12 hours in phosphate buffer solution at pH 6.0 (fig. S33) under catalytic conditions ($\mathbf{1}/[Fe^{III}(C_5Me_5)_2]^{+} = 1/300$). Significantly, this is the first example of catalytic e⁻ transfer to a substrate with a NiFe complex by using H_2 as the e⁻ source in water. The turnover number (TON) was determined as 86 at pH 6.0 by using UV-vis absorption spectroscopy. For the H⁻ transfer, $[MB]^{+}$ was catalytically reduced to leucomethylene blue (MBH) by H_2 (0.1 to 0.8 MPa), in the presence of catalytic amounts of **1**, at 30°C for 12 hours in phosphate buffer solution at pH 6.0 ($\mathbf{1}/[MB]^{+} = 1/98$). The TON was determined to be 23 (fig. S34) by using UV-vis absorption spectroscopy. Catalytic H_2 evolution was observed using methyl viologen cation radical ($[MV]^{+}$) as an e⁻ donor and acetate buffer solution (pH 4.0) as the H⁺ donor at 40°C in the presence of catalytic amounts of **1** (11 equivalents of $[MV]^{+}$). The TON was determined as 2.67 by using GC. It was confirmed by GC that D_2 was evolved from a CD_3COOD/D_2O solution of **1** and $[MV]^{+}$ at pD 4.0.

CONCLUSION

In conclusion, we have synthesized and characterized a [NiFe] H_2ase model complex, **1**, that is capable of catalyzing e⁻ transfer, H_2 evolution, and H⁻ transfer in water. Of particular note, **1** presents the first example of a NiFe complex that is capable of achieving catalytic e⁻ transfer from H_2 in water. We have also isolated and characterized three hydride isomers, **2a**, **2b**, and **2c**, and demonstrated that their relative catalytic efficiencies follow the same pattern as the efficiencies of their natural analogs. We believe that these studies will provide crucial insights into the mechanism of natural H_2ases.

Fig. 4. The e⁻ transfer (drawn in red), H_2 evolution (drawn in blue), and H⁻ transfer reactions (drawn in green) with three isomers of the hydride complexes, 2a, 2b, and 2c.

Fig. 5. The differing reactivity of the three isomers. Y', methylene blue [MB]⁺.

MATERIALS AND METHODS

All experiments were carried out under an N_2 atmosphere using standard Schlenk techniques and a glovebox. Acetonitrile was distilled over CaH_2 under an N_2 atmosphere and dried with molecular sieves 3A that was activated at 300°C for 6 hours under reduced pressure. H_2 (99.9999%), D_2 (99.5%), and CO (99.9%) were purchased from Sumitomo Seika Chemical Co. Ltd.; ultrapure water and methylene blue trihydrate {3,7-bis(dimethylamino)-5-phenothiazinium chloride trihydrate, [MB](Cl)·$3H_2O$} were purchased from FUJIFILM Wako Pure Chemical Corporation; methyl viologen {1,1′-dimethyl-4,4′-bipyridinium dichloride, [MV]$(Cl)_2$} was purchased from Tokyo Chemical Industry Co. Ltd.; $NaBH_4$ and benzaldehyde were purchased from Sigma-Aldrich; and $CDCl_3$, CD_2Cl_2, CD_3COCD_3, $NaBD_4$, D_2O, CD_3COOD, CD_3CN, and ^{13}CO gas (99%) were purchased from Cambridge Isotope Laboratories Inc. These reagents were used without further purification. Decamethylferrocene [$Fe^{II}(C_5Me_5)_2$] was purchased from FUJIFILM Wako Pure Chemical Corporation and used after purification by sublimation. [Fe^{II}(L)$(Cl)_2$] [L = 1,2-bis(diphenylphosphino)ethane], [Ni^{II}(Z)] (Z = $N,N′$-diethyl-3,7-diazanonane-1,9-dithiolato), and sodium tetrakis(m-terphenyl-5′-yl)borate ($NaBAr_4$) were prepared by the methods described in the literature (14–16). Decamethylferrocenium nitrate {[Fe^{III}($C_5Me_5)_2$](NO_3)} and methylene blue trifluoromethanesulfonate {[MB](OTf)} were synthesized by the modified literature methods (17, 18).

ESI-MS data were obtained with JEOL JMS-T100LC AccuTOF. Proton and phosphorus NMR (^1H and ^{31}P NMR) spectra were recorded on a JEOL JNM-ESC400 spectrometer. Chemical shifts in $CDCl_3$, CD_3COCD_3, CD_3CN, and CD_2Cl_2 were referenced to tetramethylsilane (TMS) for ^1H NMR and referenced to 85% phosphoric acid for ^{31}P NMR. Fourier transform IR spectra in solid states were obtained using a PerkinElmer Spectrum Two IR spectrometer with attenuated total reflectance accessory. Mössbauer spectra were measured with a WissEl MVT-1000 M Mössbauer spectrometer, in which the temperature was controlled with a temperature controller (SI9650, YOYO Co.) within a variable temperature cryostat (Iwatani Co. Ltd.). A 50-mCi cobalt-57 source diffused into a rhodium foil was used. The velocity scales and isomer shifts were normalized to iron foil at room temperature. Elemental analyses were performed using a Yanaco CHN coder (MT-5). UV-vis spectra were recorded on a JASCO V-670 UV-vis-NIR spectrophotometer. GC analyses of H_2 were conducted using a Shimadzu GC-2014 (Ar carrier) instrument with an activated charcoal column equipped with a thermal conductivity detector. GC analyses of D_2 were conducted using Shimadzu GC-8A (He carrier) with a $MnCl_2$-alumina column (model: Shinwa OGO-SP) at −196°C (liquid N_2) and equipped with a thermal conductivity detector. X-band ESR spectra of [1](Cl), [2a](PF_6), [2b](PF_6), and [2c](PF_6) in acetone at 128 K were measured using a Bruker EMX plus spectrometer.

[Ni^{II}(Z)Fe^{II}(Cl)(CO)(L)](Cl) {[1](Cl)}

All procedures were conducted under dark conditions. Acetone (25 ml) was added to a solid of [Fe^{II}(L)$(Cl)_2$] (500 mg, 0.95 mmol). Methanol (25 ml) was added to the suspension to dissolve [Fe^{II}(L)$(Cl)_2$]. The methanol solution (15 ml) of [Ni^{II}(Z)] (292 mg, 0.95 mmol) was added to the methanol/acetone solution of [Fe^{II}(L)$(Cl)_2$]. CO gas was bubbled through the resulting solution within a few minutes after the addition of [Ni^{II}(Z)]. After stirring for 30 min, the solvents were removed by evaporation at −10°C to form dark red powders

{yield: 92% based on [Fe^{II}(L)$(Cl)_2$]}. ^1H NMR (400 MHz, in $CDCl_3$, referenced to TMS): δ 1.22 to 3.86 (m, 28H, N—CH_2—CH_3, —CH_2—, N—CH_2—CH_3), 7.16 to 7.89 (m, 18H, P—C_6H_5), and 8.10 to 8.29 (m, 2H, P—C_6H_5). ^{31}P NMR (202 MHz, in $CDCl_3$, referenced to external 85% H_3PO_4): δ 64.5 (s, 1P, Fe—P) and 72.9 (s, 1P, Fe—P). ESI-MS (in methanol): m/z 823.1 {[1]$^+$, relative intensity (I) = 100% in the range of m/z 200 to 2000}. Anal. calcd for [1](Cl)·$2CH_3OH$: $C_{40}H_{56}Cl_2FeN_2NiO_3P_2S_2$: C, 51.97; H, 6.11; N, 3.03%. Found: C, 51.72; H, 6.24; N, 2.95%. IR (cm^{-1}): 1950 (ν_{CO}). UV-vis: 400 nm (ε = 4600 M^{-1} cm^{-1}).

[Ni^{II}(Z)Fe^{II}(Cl)(^{13}CO)(L)](Cl) {[^{13}CO-labeled 1](Cl)}

^{13}CO-labeled complex [^{13}CO-labeled 1](Cl) was prepared by the same method as the synthesis of [1](Cl) except the use of ^{13}CO instead of CO. ESI-MS (in methanol): m/z 824.3 {[^{13}CO-labeled 1]$^+$, I = 100% in the range of m/z 200 to 2000}. IR (cm^{-1}): 1906 (ν_{13CO}).

[Ni^{II}(Z)(μ-H)Fe^{II}(CO)(L)](PF$_6$) {[2a](PF$_6$)}

All procedures were conducted under dark conditions. Method A: A 40 mM phosphate buffer solution (pH 7.0, 35 ml) of [1](Cl) (50 mg, 58 μmol) was stirred for 2 hours under an H_2 atmosphere (0.1 to 0.8 MPa) at room temperature. KPF_6 (16 mg, 87 μmol) was added to the resulting solution to afford red-purple precipitates, which were collected by filtration and dried in vacuo {yield of mixture of three isomers: 92% based on [1](Cl)}. The red-purple precipitates were recrystallized in its acetone solution diffused by diethyl ether for 2 days at room temperature to yield the brown crystals, which were collected by filtration and dried in vacuo {yield: 66% based on [1](Cl)}. Method B: A methanol solution (4 ml) of [1](Cl) (100 mg, 116 μmol) was added to $NaBH_4$ (100 mg, 2.64 mmol), and the resulting solution was kept standing until the H_2 bubble was diminished, to which KPF_6 (64 mg, 0.35 mmol) was added. Acetone (4 ml) was added to the suspension to dissolve remaining KPF_6, and the resulting solution diffused by diethyl ether was kept standing for 2 days at room temperature to form crystals, which were obtained and collected by filtration. Dichloromethane (15 ml) was added into the crystals, and the filtrate was collected by filtration to remove the residue. The solvent was removed under reduced pressure to afford the solid, which was recrystallized in acetone/methanol (1:1) solution diffused by diethyl ether for 2 days at room temperature. Brown crystals were collected by filtration and dried in vacuo {yield: 70% based on [1](Cl)}. ^1H NMR [400 MHz, in CD_3COCD_3/CD_2Cl_2 (1:1), referenced to TMS]: δ −2.76 [dd, 1H, Ni(μ-H)Fe], −0.43 (d, 1H, S—CH_2—), 0.92 (t, 3H, N—CH_2—CH_3), 1.03 (t, 3H, N—CH_2—CH_3), 1.31 to 1.40, 1.78 to 1.99, 2.06 to 2.36, 2.45 to 2.57, 2.62 to 2.92, 3.04 to 3.73 (m, 21H, —CH_2—), 7.27 to 7.63 (m, 18H, P—C_6H_5), and 8.19 to 8.25 (m, 2H, P—C_6H_5). ^{31}P NMR (202 MHz, in CD_3COCD_3, referenced to external 85% H_3PO_4): δ 59.7 (s, 1P, Fe—P) and 95.3 (s, 1P, Fe—P). ESI-MS (in methanol): m/z 789.1 {[2a]$^+$, I = 100% in the range of m/z 200 to 2000}. Anal. calcd for [2a](PF_6): $C_{38}H_{49}F_6FeN_2NiOP_3S_2$: C, 48.79; H, 5.28; N, 2.99%. Found: C, 48.78; H, 5.38; N, 2.95%. IR (cm^{-1}): 1918 (ν_{CO}) and 1675 ($\nu_{Ni-H-Fe}$). UV-vis: 410 nm (ε = 2940 M^{-1} cm^{-1}).

[Ni^{II}(Z)Fe^{II}(CO)(L)(H)](PF$_6$) {[2b](PF$_6$)}

All procedures were conducted under dark conditions. A 40 mM phosphate buffer solution (pH 7.0, 35 ml) of [1](Cl) (50 mg, 58 μmol) was stirred for 2 hours under an H_2 atmosphere (0.1 to 0.8 MPa) at room temperature. KPF_6 (16 mg, 87 μmol) was added to the resulting

solution to afford red-purple precipitates, which were collected by filtration and dried in vacuo. The red-purple precipitates were recrystallized in acetone/methanol (1:1) solution diffused by diethyl ether for 4 days at −30°C. The brown crystals were removed by decantation at −20°C, and the solvent was removed in vacuo to form the red-purple powders at low temperature of −20°C to prevent isomerization. The recrystallization was repeated for two to three times to remove **2a** and **2c** {yield: 54% based on [**1**](Cl)}. ^{1}H NMR (400 MHz, in CD$_3$COCD$_3$, referenced to TMS): δ −3.83 (t, 1H, Fe—H), 1.33 (t, 6H, N—CH$_2$—CH_3), 3.17 (m, 4H, N—CH_2—CH$_3$), 0.88 to 1.52, 1.84 to 2.35, 2.47 to 2.98 (m, 18H, —CH_2—), 7.35 to 7.59 (m, 16H, P—C$_6H_5$), and 7.89 to 7.95 (m, 4H, P—C$_6H_5$). ^{31}P NMR (202 MHz, in CD$_3$COCD$_3$, referenced to external 85% H$_3$PO$_4$): δ 96.3 (s, 2P, Fe—P). ESI-MS (in methanol): m/z 789.2 {[**2b**]$^+$, $I = 100\%$ in the range of m/z 200 to 2000}. Anal. calcd for [**2b**](PF$_6$): C$_{38}$H$_{49}$F$_6$FeN$_2$NiOP$_3$S$_2$: C, 48.79; H, 5.28; N, 2.99%. Found: C, 48.87; H, 5.40; N, 2.97%. UV-vis: 500 nm (ε = 1040 M^{-1} cm^{-1}).

[Ni^{II}(Z)Fe^{II}(CO)(L)(H)](BAr$_4$) {[2b](BAr$_4$)}

All procedures were conducted under dark conditions. A 40 mM phosphate buffer solution (pH 7.0, 70 ml) of [**1**](Cl) (100 mg, 116 μmol) was stirred for 2 hours under an H$_2$ atmosphere (0.1 to 0.8 MPa) at room temperature. Methanol solution (15 ml) of NaBAr$_4$ (132 mg, 0.139 mmol) was added to the resulting solution to afford pale purple precipitates, which were collected by filtration and dried in vacuo. The pale purple precipitates were recrystallized by the slow vapor diffusion of diethyl ether into its acetone solution (17.5 mM) for 10 hours at −30°C. Red-purple crystals were collected by filtration and dried in vacuo {yield: 13% based on [**1**](Cl)}. ^{1}H NMR (400 MHz, in CD$_3$COCD$_3$, referenced to TMS): δ −3.83 (t, 1H, Fe—H), 1.33 (t, 6H, N—CH$_2$—CH_3), 3.17 (m, 4H, N—CH_2—CH$_3$), 1.31 to 1.52, 1.84 to 2.35, 2.47 to 2.98 (m, 18H, —CH_2—), 7.18 (t, 8H, BAr$_4$), 7.31 (t, 16H, BAr$_4$), 7.43 to 7.56 (m, 16H, P—C$_6H_5$), 7.65 (d, 16H, BAr$_4$), 7.90 (t, 4H, P—C$_6H_5$), and 8.12 (s, 8H, BAr$_4$). Anal. calcd for [**2b**](BAr$_4$)·5H$_2$O: C$_{110}$H$_{111}$BFeN$_2$NiO$_6$P$_2$S$_2$: C, 73.05; H, 6.19; N, 1.55%. Found: C, 72.79; H, 5.89; N, 1.44%. IR (cm^{-1}): 1910 (ν$_{CO}$) and 543 (δ$_{H–Fe–CO}$).

[Ni^{II}(Z)Fe^{II}(CO)(L)(H)](PF$_6$) {[2c](PF$_6$)}

All procedures were conducted under dark conditions. Method A: A 40 mM phosphate buffer solution (pH 7.0, 70 ml) of [**1**](Cl) (100 mg, 116 μmol) was stirred for 2 hours under an H$_2$ atmosphere (0.1 to 0.8 MPa) at room temperature. KPF$_6$ (32 mg, 0.174 mmol) was added to the resulting solution to afford red-purple precipitates, which were collected by filtration and dried in vacuo. The red-purple precipitates were recrystallized by slow vapor diffusion of diethyl ether (40 ml) into its acetone solution (7 ml) at −30°C for 2 days to generate red-brown crystals. The red-brown crystals were removed by decantation, and the solvent was removed under reduced pressure. The residue was dissolved in acetone (1 ml), and methanol (1 ml) was added into the acetone solution. The resulting solution (2 ml) was diffused by cooled diethyl ether (20 ml), and it was kept standing at −30°C for 3 days. The brown crystals were collected by filtration and were dissolved in acetone (2 ml). The insoluble materials were removed by decantation, and the resulting solution (2 ml) was diffused by cooled diethyl ether (20 ml), and it was kept standing at −30°C for 3 days. The brown crystals were removed by decantation, and the solvent was removed under reduced pressure. The residue was dissolved in acetone (0.3 ml), to which methanol (0.2 ml) was added. The

resulting solution (0.5 ml) was diffused by cooled diethyl ether (20 ml) and was kept standing at −30°C for 2 days. The brown solid was collected by filtration and dried in vacuo {yield: 7% based on [**1**](Cl)}. Method B: A methanol solution (15 ml) of [**1**](Cl) (200 mg, 232 μmol) was added to NaBH$_4$ (400 mg, 10.6 mmol) at room temperature. The resulting solution was kept standing until H$_2$ gas diminished and was added to KPF$_6$ (128 mg, 695 μmol). Acetone (7 ml) was added to the resulting suspension to dissolve remaining KPF$_6$. The resulting solution diffused by diethyl ether (90 ml) was kept standing at −30°C for 1 day to form [**2a**](PF$_6$) and inorganic salts. The precipitates were removed by decantation, and the solvent was removed under reduced pressure. Dichloromethane (20 ml) was added into the residue, and the insoluble materials were removed by filtration. The solvent was removed under reduced pressure at low temperature. The residue (ca. 100 mg) was dissolved in acetone (1 ml), to which methanol (1 ml) was added. The resulting solution (2 ml) was diffused by cooled diethyl ether (20 ml) and was kept standing at −30°C for 3 days. Brown crystals (ca. 60 mg) were collected by filtration and were dissolved in acetone (6 ml). The acetone solution was diffused by cooled diethyl ether (60 ml) and was kept standing at −30°C for 2 days. Brown crystals were removed by decantation, and the solvent was removed under reduced pressure at low temperature. The residue (ca. 25 mg) was dissolved into acetone (1 ml), to which methanol (0.7 ml) was added. The resulting solution (1.7 ml) was diffused by cooled diethyl ether (20 ml) and was kept standing at −30°C for 2 days. The brown solid was collected by filtration and dried in vacuo {yield: 6% based on [**1**](Cl)}. ^{1}H NMR (400 MHz, in CD$_3$COCD$_3$, referenced to TMS): δ −16.62 (dd, 1H, Fe—H), 1.03 (t, 3H, N—CH$_2$—CH_3), 1.23 (t, 3H, N—CH$_2$—CH_3), 0.87 to 1.88, 2.39 to 3.69 (m, 22H, —CH_2—), and 7.47 to 7.94 (m, 20H, P—C$_6H_5$). ^{31}P NMR (202 MHz, in CD$_3$COCD$_3$, referenced to external 85% H$_3$PO$_4$): δ 76.3 (s, 1P, Fe—P) and 102.4 (s, 1P, Fe—P). ESI-MS (in methanol): m/z 789.1 {[**2c**]$^+$, $I = 100\%$ in the range of m/z 200 to 2000}. Anal. calcd for [**2c**](PF$_6$): C$_{38}$H$_{49}$F$_6$FeN$_2$NiOP$_3$S$_2$: C, 48.79; H, 5.28; N, 2.99%. Found: C, 48.63; H, 5.19; N, 3.00%. IR (cm^{-1}): 1885 (ν$_{CO}$) and 1964 (ν$_{Fe-H}$). UV-vis: 400 nm (ε = 2130 M^{-1} cm^{-1}).

[Ni^{II}(Z)(μ-D)Fe^{II}(CO)(L)](PF$_6$) {[D-labeled 2a](PF$_6$)}

Deuteride complex [D-labeled **2a**](PF$_6$) was prepared by the same method as the synthesis of [**2a**](PF$_6$) except the use of D$_2$ or NaBD$_4$ instead of H$_2$ (method A) or NaBH$_4$ (method B). ESI-MS (in methanol): m/z 790.3 {[D-labeled **2a**]$^+$, $I = 100\%$ in the range of m/z 200 to 2000}. IR (cm^{-1}): 1918 (ν$_{CO}$) and 1212 (ν$_{Ni-D-Fe}$).

[Ni^{II}(Z)Fe^{II}(CO)(L)(D)](PF$_6$) {[D-labeled 2b](PF$_6$)}

Deuteride complex [D-labeled **2b**](PF$_6$) was prepared by the same method as the synthesis of [**2b**](PF$_6$) except the use of D$_2$ instead of H$_2$. ESI-MS (in methanol): m/z 790.3 {[D-labeled **2b**]$^+$, $I = 100\%$ in the range of m/z 200 to 2000}.

[Ni^{II}(Z)Fe^{II}(CO)(L)(D)](BAr$_4$) {[D-labeled 2b](BAr$_4$)}

Deuteride complex [D-labeled **2b**](BAr$_4$) was prepared by the same method as the synthesis of [**2b**](BAr$_4$) except the use of D$_2$ instead of H$_2$. ESI-MS (in methanol): m/z 790.2 {[D-labeled **2b**]$^+$, $I = 100\%$ in the range of m/z 200 to 2000}. IR (cm^{-1}): 1904 (ν$_{CO}$) and 531 (δ$_{D-Fe-CO}$).

[Ni^{II}(Z)Fe^{II}(CO)(L)(D)](PF$_6$) {[D-labeled 2c](PF$_6$)}

Deuteride complex [D-labeled **2c**](PF$_6$) was prepared by the same method (method A) as the synthesis of [**2c**](PF$_6$) except the use of

D$_2$ instead of H$_2$. ESI-MS (in methanol): m/z 790.2 {[D-labeled **2c**]$^+$, I = 100% in the range of m/z 200 to 2000}. IR (cm^{-1}): 1886 (v_{CO}) and 1414 (v_{Fe-D}).

H$_2$ activation by 1 in water to form three hydride isomers monitored by ESI-MS

All procedures were conducted under dark conditions. A 40 mM phosphate buffer solution (pH 7.0, 10 ml) of [**1**](Cl) (1.2 mg, 1.4 μmol) was stirred for 2 hours under an H$_2$ atmosphere (0.1 MPa) at room temperature. A portion (200 μl) of the resulting aqueous solution was diluted by methanol (1 ml), which was analyzed by ESI-MS.

H$_2$ activation by 1 in water to form three hydride isomers monitored by ^{1}H NMR spectroscopy

All procedures were conducted under dark conditions. A 40 mM phosphate buffer solution (pH 6.0, 35 ml) of [**1**](Cl) (50 mg, 58 μmol) was stirred for 4 hours under an H$_2$ atmosphere (0.8 MPa) at room temperature. KPF$_6$ (32 mg, 0.174 mmol) was added to the resulting solution to afford red-purple precipitates of [**2a**](PF$_6$), [**2b**](PF$_6$), and [**2c**](PF$_6$), which were collected by filtration and dried in vacuo. The precipitates (5 mg) were dissolved into CD$_3$COCD$_3$ (480 μl), which was analyzed by ^{1}H NMR spectroscopy.

Time profiles for the ratios of isomers 2a, 2b, and 2c monitored by ^{1}H NMR spectroscopy

Hydride complex [**2a**](PF$_6$), [**2b**](PF$_6$), or [**2c**](PF$_6$) (3.0 mg, 3.21 μmol) was dissolved to CD$_3$COCD$_3$ (480 μl), whose isomerization at room temperature was monitored by ^{1}H NMR spectroscopy to follow each hydride peak. Kinetic analyses were conducted by least-square curve fittings based on the data and selected rate equations of figs. S23 and S25.

[MV]$_2$(ZnCl$_4$)

Zinc powder (50 mg, 0.76 mmol) was added to an aqueous solution of methyl viologen {1,1′-dimethyl-4,4′-bipyridinium dichloride, [MV](Cl)$_2$} (300 mg, 1.17 mmol). The resulting suspension was stirred for 15 min, and the insoluble materials were removed by filtration. The filtrate was added to a saturated NaCl aqueous solution (10 ml) to form purple precipitates, which were collected by filtration and dried in vacuo {yield: 43% based on [MV](Cl)$_2$}. Anal. calcd for [MV]$_2$(ZnCl$_4$)·1.2H$_2$O: C$_{24}$H$_{30.4}$Cl$_4$N$_2$O$_{1.2}$Zn: C, 47.94; H, 5.10; N, 9.32%. Found: C, 47.84; H, 4.89; N, 9.29%. The [MV]$^+$ was confirmed by UV-vis spectroscopy (*19*).

[MB](OTf)

[MB](OTf) was synthesized by the modified literature method (*18*). Methylene blue trihydrate {3,7-bis(dimethylamino)-5-phenothiazinium chloride trihydrate, [MB](Cl)·3H$_2$O} (300 mg, 0.802 mmol) was dissolved into water (100 ml), and the insoluble materials were removed by filtration. To the filtrate, sodium trifluoromethanesulfonate (414 mg, 2.41 mmol) was added. Dark blue solids were collected by filtration and dried under reduced pressure {yield: 68% based on [MB](Cl)·3H$_2$O}. Anal. calcd for [MB](OTf)·1.5H$_2$O: C$_{17}$H$_{21}$F$_3$N$_3$O$_{4.5}$S$_2$: C, 44.34; H, 4.60; N, 9.13%. Found: C, 44.36; H, 4.33; N, 9.11%.

Decamethylferrocenium nitrate {[Fe^{III}(C$_5$Me$_5$)$_2$](NO$_3$)}

[Fe^{III}(C$_5$Me$_5$)$_2$](NO$_3$) was synthesized by using the modified literature method (*17*). Ag(NO$_3$) (161 mg, 0.948 mmol) in water (20 ml) was added to an acetone (100 ml) solution of decamethylferrocene [Fe^{II}(C$_5$Me$_5$)$_2$] (311 mg, 0.953 mmol), and the resulting solution was stirred for 4 hours at room temperature. Gray precipitates were removed by filtration, and the filtrate was evaporated up to 10 ml. Insoluble materials were removed by filtration, and the solvent was removed from the filtrate under reduced pressure. Dichloromethane was added into the residue, and the insoluble materials were removed by filtration. The solvent was evaporated to obtain green power (yield: 73% based on [Fe^{II}(C$_5$Me$_5$)$_2$]). Anal. calcd for [Fe^{III}(C$_5$Me$_5$)$_2$](NO$_3$): C$_{20}$H$_{30}$FeNO$_3$: C, 61.86; H, 7.79; N, 3.61%. Found: C, 61.63; H, 7.82; N, 3.59%.

Stoichiometric reduction of [Fe^{III}(C$_5$Me$_5$)$_2$]$^+$ with 2a, 2b, or 2c in the absence of H$_2$

An acetonitrile solution (50 μl) of [**2a**](PF$_6$), [**2b**](PF$_6$), or [**2c**](PF$_6$) (1.0 mg, 1.07 μmol) was added to an acetonitrile solution (50 μl) of [Fe^{III}(C$_5$Me$_5$)$_2$](NO$_3$) (0.83 mg, 2.14 μmol). The resulting solution was kept standing for 1 min at room temperature, which results in the reduction of [Fe^{III}(C$_5$Me$_5$)$_2$]$^+$. The resulting solution was diluted to 300 μl by acetonitrile, which was monitored by UV-vis absorption spectroscopy {absorption band at 778 nm derived from [Fe^{II}(C$_5$Me$_5$)$_2$]$^+$} to confirm the reduction of [Fe^{III}(C$_5$Me$_5$)$_2$]$^+$ to form [Fe^{II}(C$_5$Me$_5$)$_2$]. The yields of [Fe^{II}(C$_5$Me$_5$)$_2$] were determined as 57% for **2a**, 27% for **2b**, and 33% for **2c** based on **2a**, **2b**, and **2c** by UV-vis absorption spectroscopy {yield = (mol of [Fe^{II}(C$_5$Me$_5$)$_2$]/mol of **2a**, **2b**, or **2c**)/2 × 100% because of two-electron donor of **2a**, **2b**, and **2c** and one-electron acceptor of [Fe^{III}(C$_5$Me$_5$)$_2$]$^+$}, respectively. No reduction of [Fe^{III}(C$_5$Me$_5$)$_2$]$^+$ occurred without **2a**, **2b**, or **2c**, which was confirmed by UV-vis absorption spectroscopy.

Stoichiometric H$_2$ evolution from the reaction of 2a, 2b, or 2c with proton of acetic acid

In 2.0-ml vial capped with septum, an aqueous acetic acid solution (0.1 M, 300 μl) was added to an acetonitrile solution (330 μl) of [**2a**](PF$_6$), [**2b**](PF$_6$), or [**2c**](PF$_6$) (1.0 mg, 1.07 μmol), and the resulting solution was standing for 30 min at room temperature. The evolved H$_2$ in the gas phase of the vial was sampled by a gas-tight syringe and quantified by GC. The yields were determined to be 16% for **2a**, 55% for **2b**, and 9% for **2c**, based on [**2a**](PF$_6$), [**2b**](PF$_6$), and [**2c**](PF$_6$) [yield = (mol of H$_2$/mol of **2a**, **2b**, or **2c**) × 100%], respectively. No H$_2$ was formed without **2a**, **2b**, **2c**, or acetic acid, which was confirmed by GC as blank experiment.

Stoichiometric reduction of [MB]$^+$ with 2a in the absence of H$_2$

An acetonitrile solution (98 μl, 21.5 mM) of [MB](OTf) was added to [**2a**](PF$_6$) (0.98 mg, 1.05 μmol), and the resulting solution was kept standing for 60 min at room temperature, which results in the reduction of [MB]$^+$ to MBH. Dichloromethane (2.0 ml) was added to a portion (10 μl) of the solution, which was measured by UV-vis absorption spectroscopy (absorption band at 654 nm derived from [MB]$^+$). The yield of MBH was determined as 4% based on **2a** by UV-vis absorption spectroscopy [yield = (mol of MBH/mol of **2a**) × 100%]. No reduction of [MB]$^+$ occurred without **2a**, which was confirmed by UV-vis absorption spectroscopy as blank experiment.

Stoichiometric reduction of [MB]$^+$ with 2b in the absence of H$_2$

An acetonitrile solution (121 μl, 21.5 mM) of [MB](OTf) was added to [**2b**](PF$_6$) (1.21 mg, 1.29 μmol), and the resulting solution was

kept standing for 60 min at room temperature, which results in the reduction of $[MB]^+$ to MBH. Dichloromethane (2.0 ml) was added to a portion (10 µl) of the solution, which was measured by UV-vis absorption spectroscopy (absorption band at 654 nm derived from $[MB]^+$). The yield of MBH was determined as 14% based on **2b** by UV-vis absorption spectroscopy [yield = (mol of MBH/mol of **2b**) × 100%]. No reduction of $[MB]^+$ occurred without **2b**, which was confirmed by UV-vis absorption spectroscopy as blank experiment.

Stoichiometric reduction of $[MB]^+$ with 2c in the absence of H_2
An acetonitrile solution (111 µl, 21.5 mM) of [MB](OTf) was added to [**2c**](PF$_6$) (1.11 mg, 1.19 µmol), and the resulting solution was kept standing for 60 min at room temperature, which results in the reduction of $[MB]^+$ to MBH. Dichloromethane (2.0 ml) was added to a portion (10 µl) of the solution, which was measured by UV-vis absorption spectroscopy (absorption band at 654 nm derived from $[MB]^+$). The yield of MBH was determined as 31% based on **2c** by UV-vis absorption spectroscopy [yield = (mol of MBH/mol of **2c**) × 100%]. No reduction of $[MB]^+$ occurred without **2c**, which was confirmed by UV-vis absorption spectroscopy as blank experiment.

Time profiles for isomerization of 2b to 2a and 2c with or without proton from acetic acid monitored by ^{1}H NMR spectroscopy
Hydride complex [**2b**](PF$_6$) (2.0 mg, 2.14 µmol) was dissolved into the mixture of CD$_3$CN (160 µl) and aqueous acetic acid solution (0.8 M, 50 µl). The isomerization process at room temperature was monitored by ^{1}H NMR spectroscopy based on each hydride signal. A sealed capillary tube within benzaldehyde (10 mM) in CD$_3$CN as a standard reference material was set in an NMR tube. The isomerization process of **2b** without acid-derived proton in CD$_3$CN/H$_2$O was monitored by ^{1}H NMR spectroscopy in the mixture solution of CD$_3$CN (80 µl) and H$_2$O (25 µl) containing [**2b**](PF$_6$) (1.0 mg, 1.07 µmol). On the basis of the data and selected rate equations of figs. S24 and S25, kinetic analyses were conducted by least-square curve fittings.

Time profiles for isomerization of 2c to 2a with or without $[MB]^+$ monitored by ^{1}H NMR spectroscopy
An CD$_3$CN (200 µl) solution of [MB](OTf) (1.86 mg, 4.29 µmol) was added into the hydride complex [**2c**](PF$_6$) (2.0 mg, 2.14 µmol). The isomerization process at room temperature was monitored by ^{1}H NMR spectroscopy based on each hydride peak. A sealed capillary tube within benzaldehyde (10 mM) in CD$_3$CN as a standard reference material was set in an NMR tube. The isomerization process of **2c** without $[MB]^+$ in CD$_3$CN was monitored by ^{1}H NMR spectroscopy in the CD$_3$CN solution (100 µl) of [**2c**](PF$_6$) (1.0 mg, 1.07 µmol). The rate constants were determined by least-square curve fittings based on the data and selected rate equations of figs. S24 and S25.

Catalytic reduction of $[Fe^{III}(C_5Me_5)_2]^+$ with 1 in the presence of H_2
All procedures were conducted under dark conditions. A 40 mM phosphate buffer solution (pH 6.0, 2.0 ml) of [**1**](Cl) (0.03 mg, 0.0174 mM) and [Fe^{III}(C$_5$Me$_5$)$_2$](NO$_3$) (4.06 mg, 5.23 mM) was stirred under an H_2 atmosphere (0.8 MPa) at 50°C for 12 hours. The resulting solution was filtrated to remove [Fe^{II}(C$_5$Me$_5$)$_2$] formed and was monitored by UV-vis absorption spectroscopy {absorption band at 778 nm derived from [Fe^{III}(C$_5$Me$_5$)$_2$]$^+$}. The TON of the reduction of [Fe^{III}(C$_5$Me$_5$)$_2$]$^+$ was determined to be 86 by UV-vis absorption spectroscopy {TON = (mol of [Fe^{II}(C$_5$Me$_5$)$_2$]/mol of **1**)/2 because of two-electron donor of the hydride complex and one-electron acceptor of [Fe^{III}(C$_5$Me$_5$)$_2$]$^+$}. No catalytic reduction of [Fe^{III}(C$_5$Me$_5$)$_2$]$^+$ occurred without **1** or H_2, which was confirmed by UV-vis absorption spectroscopy as blank experiment. Complex **1** was stable under the conducted conditions, which was confirmed by ESI-MS.

Catalytic H_2 evolution with 1 in the presence of $[MV]^+$ as an electron source
All procedures were conducted under dark conditions. In 3.0-ml vial capped with septum, a 100 mM acetate buffer solution (pH 4.0, 2.0 ml) of [**1**](Cl) (1.0 mg, 0.58 mM) and [MV]$_2$(ZnCl$_4$) (7.7 mg, 6.64 mM) was stirred for 6 hours at 40°C. The evolved H_2 in the gas phase of the vial was sampled by a gas-tight syringe and quantified by GC. The TON of the H_2 evolution was determined as 2.67 by GC (TON = mol of H_2/mol of **1**). No catalytic evolution of H_2 occurred without **1** or [MV]$_2$(ZnCl$_4$), which was confirmed by GC as blank experiment. It was confirmed that **1** was stable under the conducted conditions by ESI-MS.

D_2 evolution with 1 in the presence of $[MV]^+$ as an electron source
All procedures were conducted under dark conditions. In 3.0-ml vial capped with septum, a CD$_3$COOD solution in D$_2$O (pD 4.0, 2.0 ml) of [**1**](Cl) (1.0 mg, 0.58 mM) and [MV]$_2$(ZnCl$_4$) (7.7 mg, 6.64 mM) was kept standing for 5 hours at 40°C. The evolved D_2 in the gas phase of the vial was sampled by a gas-tight syringe by GC. No D_2 was formed without **1** or [MV]$_2$(ZnCl$_4$), which was confirmed by GC as blank experiment.

Catalytic reduction of $[MB]^+$ with 1 in the presence of H_2
All procedures were conducted under dark conditions. A 37.5 mM phosphate buffer solution (pH 6.0, 2.0 ml) of [**1**](Cl) (0.11 mg, 0.064 mM) and [MB](Cl)·3H$_2$O (4.67 mg, 6.25 mM) was stirred under an H_2 atmosphere (0.8 MPa) at room temperature or at 30°C for 12 hours. A portion (50 µl) of the resulting solution was diluted with 2 ml of water, which was monitored by UV-vis absorption spectroscopy (absorption band at 664 nm derived from $[MB]^+$). The TON of the reduction of $[MB]^+$ was determined as 23 by UV-vis absorption spectroscopy (TON = mol of MBH/mol of **1**). No catalytic reduction of $[MB]^+$ occurred without **1** or H_2, which was confirmed by UV-vis absorption spectroscopy as blank experiment. No decomposition of **1** was observed under the conducted conditions, which was confirmed by ESI-MS.

Electrochemical analysis
Electrochemical measurements were conducted in an acetonitrile solution of each hydride complex [**2a**](PF$_6$), [**2b**](PF$_6$), or [**2c**](PF$_6$) (1.0 mM) with ^{n}Bu$_4$NPF$_6$ (^{n}Bu = normal butyl) (0.1 M) as a supporting electrolyte on a BAS660A electrochemical analyzer using a carbon working electrode at room temperature. The cyclic voltammograms were collected using a scan rate of 100 mV s^{-1}. Potentials are referenced to a Fc$^+$/Fc (ferrocenium/ferrocene) couple.

pH adjustment
pH values of aqueous solutions were adjusted by using acetate buffer solution for pH 4.0 and by using phosphate buffer solution for pH

6.0 to 7.0. In a pH range of 4.0 to 7.0, the pH values of the solutions were determined by a pH meter (IQ Scientific Instruments Inc., IQ200) equipped with a stainless steel micro pH probe (IQ Scientific Instruments Inc., PH15-SS). Values of pD were corrected by adding 0.4 to the observed pH values (pD = pH meter reading + 0.4) (20, 21).

Computational details

Geometry optimizations and potential energy calculations were performed for experimentally trapped four complexes, **1**, **2a**, **2b**, and **2c**, using the Gaussian 09 program (22). The experimentally determined oxidation states on the Ni and Fe species are both 2$^+$ for all four complexes, indicating that the orbital occupancies are d^8 for Ni and d^6 for Fe, respectively. Therefore, we considered four spin multiplicities ($S = 0$ to 3) to determine the ground-state spin multiplicity. All the structures were fully optimized without any constraints using the Becke-Perdew 1986 (BP86) (23, 24) functional with Grimme's (D3) dispersion correction (25). The BP86 functional has been used to model biomimetic NiFe complexes (26–29). Furthermore, in our previously studied analogical NiFe complexes, the BP86 functional correctly described the ground-state spin multiplicity, while two hybrid functionals, B3LYP-D3 (D3-corrected Becke three-parameter Lee-Yang-Parr functional) (23, 30) and TPSSh (Tao-Perdew-Staroverov-Scuseria) (31), failed to predict (32, 33). Thus, the choice of BP86 functional is appropriate. The Stuttgart-Dresden (SDD) (34) basis set and the associated effective core potential were used for Ni and Fe, and the def2-SVP(split valence polarization) basis sets (35) were applied for other atoms (BS1). The potential energies were calculated at the level of BP86-D3/BS2 (BS2 = SDD for Ni and Fe, and def2-TZVP for the other atoms). Solvation effects were considered using the solvent model density implicit solvation model (36) with acetone as the solvent (ε = 20.493) in both geometry optimizations and potential energy calculations. Vibrational frequency calculations were performed at the same level of theory to confirm minima and to obtain zero-point vibrational energy corrections. Thermal corrections were computed at the reaction conditions, that is, 298.15 K (room temperature) and 1 atm pressure. Integrals were evaluated using the pruned grid consisting of 99 radial shells and 590 angular points per shell. The wave function stability was checked for all complexes.

The ^{57}Fe Mössbauer isomer shift and quadrupole splitting were calculated using the ORCA 4.0.1 program package (37). The isomer shift shows the linear relationship with electron density at the Fe nucleus (38)

$$\text{Isomer shift} = \alpha(\rho - C) + \beta$$

where ρ is the electron density, and α, β, and C are parameters for the linear fits. The Mössbauer parameters were calculated based on the x-ray structures. We used the CP(PPP) basis set for Fe (39, 40), which performs reliably for Fe complexes (41), and the def2-TZVP basis set was used for the remaining atoms. As the hybrid density functionals give more reliable results, the TPSSh functional (31) was used. Increased integration accuracy (Grid7 for Fe and Grid6 for the reset of atoms in ORCA convention) was applied. The parameters used to drive the isomer shift, α, β, and C, are −0.376, 4.130, and 11810, respectively (41).

X-ray crystallographic analyses of 1, 2a, 2b, and 2c

A single crystal of [**1**](Cl) was obtained from its methanol solution diffused with diethyl ether at −30°C. A single crystal of [**2a**](PF$_6$) was obtained from ethanol/acetone (1:1) solution diffused with diethyl ether at room temperature. A single crystal of [**2b**](BAr$_4$) was obtained from its acetone solution diffused with diethyl ether at −30°C. A single crystal of [**2c**](PF$_6$) was obtained from its methanol/acetone (3:1) solution diffused with diethyl ether at −30°C. Measurements were made on Rigaku XtaLAB P200 with confocal monochromated Mo-Kα radiation (λ = 0.7107 Å). Data were collected and processed using the CrystalClear program. All calculations were performed using the CrystalStructure crystallographic software package.

REFERENCES AND NOTES

1. S. Ding, P. Ghosh, A. M. Lunsford, N. Wang, N. Bhuvanesh, M. B. Hall, M. Y. Darensbourg, Hemilabile bridging thiolates as proton shuttles in bioinspired H$_2$ production electrocatalysts. *J. Am. Chem. Soc.* **138**, 12920–12927 (2016).
2. T. R. Simmons, G. Berggren, M. Bacchi, M. Fontecave, V. Artero, Mimicking hydrogenases: From biomimetics to artificial enzymes. *Coord. Chem. Rev.* **270–271**, 127–150 (2014).
3. R. M. Bullock, M. L. Helm, Molecular electrocatalysts for oxidation of hydrogen using earth-abundant metals: Shoving protons around with proton relays. *Acc. Chem. Res.* **48**, 2017–2026 (2015).
4. B. C. Manor, T. B. Rauchfuss, Hydrogen activation by biomimetic [NiFe]-hydrogenase model complex containing protected cyanide cofactors. *J. Am. Chem. Soc.* **135**, 11895–11900 (2013).
5. W. Lubitz, H. Ogata, O. Rüdiger, E. Reijerse, Hydrogenases. *Chem. Rev.* **114**, 4081–4148 (2014).
6. J. A. Cracknell, K. A. Vincent, F. A. Armstrong, Enzymes as working or inspirational electrocatalysts for fuel cells and electrolysis. *Chem. Rev.* **108**, 2439–2461 (2008).
7. C. Tard, C. J. Pickett, Structural and functional analogues of the active sites of the [Fe]-, [NiFe]-, and [FeFe]-hydrogenases. *Chem. Rev.* **109**, 2245–2274 (2009).
8. S. Ogo, K. Ichikawa, T. Kishima, T. Matsumoto, H. Nakai, K. Kusaka, T. Ohhara, A functional [NiFe]hydrogenase mimic that catalyzes electron and hydride transfer from H$_2$. *Science* **339**, 682–684 (2013).
9. S. Ogo, R. Kabe, K. Uehara, B. Kure, T. Nishimura, S. C. Menon, R. Harada, S. Fukuzumi, Y. Higuchi, T. Ohhara, T. Tamada, R. Kuroki, A dinuclear Ni(μ-H)Ru complex derived from H$_2$. *Science* **316**, 585–587 (2007).
10. A. Kochem, E. Bill, F. Neese, M. van Gastel, Mössbauer and computational investigation of a functional [NiFe] hydrogenase model complex. *Chem. Commun.* **51**, 2099–2102 (2015).
11. H. Ogata, K. Nishikawa, W. Lubitz, Hydrogens detected by subatomic resolution protein crystallography in a [NiFe] hydrogenase. *Nature* **520**, 571–574 (2015).
12. H. Ogata, T. Krämer, H. Wang, D. Schilter, V. Pelmenschikov, M. van Gastel, F. Neese, T. B. Rauchfuss, L. B. Gee, A. D. Scott, Y. Yoda, Y. Tanaka, W. Lubitz, S. P. Cramer, Hydride bridge in [NiFe]-hydrogenase observed by nuclear resonance vibrational spectroscopy. *Nat. Commun.* **6**, 7890 (2015).
13. J. I. van der Vlugt, T. B. Rauchfuss, C. M. Whaley, S. R. Wilson, Characterization of a diferrous terminal hydride mechanistically relevant to the Fe-only hydrogenases. *J. Am. Chem. Soc.* **127**, 16012–16013 (2005).
14. D. J. Evans, P. B. Hitchcock, G. Jeffery Leigh, B. K. Nicholson, A. C. Niedwieski, F. S. Nunes, J. F. Soares, The synthesis of *triangulo*-trimetal complexes containing both iron(II) and vanadium(II). *Inorg. Chim. Acta* **319**, 147–158 (2001).
15. F. Osterloh, W. Saak, S. Pohl, Unidentate and bidentate binding of nickel(II) complexes to an Fe$_4$S$_4$ cluster via bridging thiolates: Synthesis, crystal structures, and electrochemical properties of model compounds for the active sites of nickel containing CO dehydrogenase/acetyl-CoA synthase. *J. Am. Chem. Soc.* **119**, 5648–5656 (1997).
16. K. Matsumoto, K. Hatano, N. Umezawa, T. Higuchi, Synthesis of a new, bulky tetraarylphosphonium, a tetraarylborate, and their salt. *Synthesis* **13**, 2181–2185 (2004).
17. S. Hamada, Y. Funasako, T. Mochida, D. Kuwahara, K. Yoza, Phase transitions and thermal properties of decamethylferrocenium salts with perfluoroalkyl-sulfonate and -carboxylate anions exhibiting disorder. *J. Organomet. Chem.* **713**, 35–41 (2012).
18. A. Costa, C. Lourenço, I. Marrucho, L. C. Branco, Alternative methods for preparation of gluconate salts using heterogeneous non-metal catalysts. *J. Mater. Sci. Eng. B* **3**, 386–392 (2013).
19. T. Watanabe, K. Honda, Measurement of the extinction coefficient of the methyl viologen cation radical and the efficiency of its formation by semiconductor photocatalysis. *J. Phys. Chem.* **86**, 2617–2619 (1982).

20. P. K. Glasoe, F. A. Long, Use of glass electrodes to measure acidities in deuterium oxide. *J. Phys. Chem.* **64**, 188–190 (1960).

21. K. Mikkelsen, S. O. Nielsen, Acidity measurements with the glass electrode in H_2O-D_2O mixtures. *J. Phys. Chem.* **64**, 632–637 (1960).

22. M. J. Frisch, G. W. Trucks, H. B. Schlegel, G. E. Scuseria, M. A. Robb, J. R. Cheeseman, G. Scalmani, V. Barone, B. Mennucci, G. A. Petersson, H. Nakatsuji, M. Caricato, X. Li, H. P. Hratchian, A. F. Izmaylov, J. Bloino, G. Zheng, J. L. Sonnenberg, M. Hada, M. Ehara, K. Toyota, R. Fukuda, J. Hasegawa, M. Ishida, T. Nakajima, Y. Honda, O. Kitao, H. Nakai, T. Vreven, J. A. Montgomery, Jr., J. E. Peralta, F. Ogliaro, M. Bearpark, J. J. Heyd, E. Brothers, K. N. Kudin, V. N. Staroverov, R. Kobayashi, J. Normand, K. Raghavachari, A. Rendell, J. C. Burant, S. S. Iyengar, J. Tomasi, M. Cossi, N. Rega, J. M. Millam, M. Klene, J. E. Knox, J. B. Cross, V. Bakken, C. Adamo, J. Jaramillo, R. Gomperts, R. E. Stratmann, O. Yazyev, A. J. Austin, R. Cammi, C. Pomelli, J. W. Ochterski, R. L. Martin, K. Morokuma, V. G. Zakrzewski, G. A. Voth, P. Salvador, J. J. Dannenberg, S. Dapprich, A. D. Daniels, Ö. Farkas, J. B. Foresman, J. V. Ortiz, J. Cioslowski, D. J. Fox, *Gaussian 09, Revision D.01; Gaussian, Inc.: Wallingford, CT*, (2009).

23. J. P. Perdew, Density-functional approximation for the correlation energy of the inhomogeneous electron gas. *Phys. Rev. B* **33**, 8822–8824 (1986).

24. A. D. Becke, Density functional calculations of molecular bond energies. *J. Chem. Phys.* **84**, 4524–4529 (1986).

25. S. Grimme, J. Antony, S. Ehrlich, H. Krieg, A consistent and accurate ab initio parametrization of density functional dispersion correction (DFT-D) for the 94 elements H-Pu. *J. Chem. Phys.* **132**, 154104 (2010).

26. M. Kampa, M. E. Pandelia, W. Lubitz, M. van Gastel, F. Neese, A metal–metal bond in the light-induced state of [NiFe] hydrogenases with relevance to hydrogen evolution. *J. Am. Chem. Soc.* **135**, 3915–3925 (2013).

27. M. Bruschi, M. Tiberti, A. Guerra, L. De Gioia, Disclosure of key stereoelectronic factors for efficient H_2 binding and cleavage in the active site of [NiFe]-hydrogenases. *J. Am. Chem. Soc.* **136**, 1803–1814 (2014).

28. P. Jayapal, M. Sundararajan, I. H. Hillier, N. A. Burton, QM/MM studies of Ni–Fe hydrogenases: The effect of enzyme environment on the structure and energies of the inactive and active states. *Phys. Chem. Chem. Phys.* **10**, 4249–4257 (2008).

29. M. G. Delcey, K. Pierloot, Q. M. Phung, S. Vancoillie, R. Lindh, U. Ryde, Accurate calculations of geometries and singlet–triplet energy differences for active-site models of [NiFe] hydrogenase. *Phys. Chem. Chem. Phys.* **16**, 7927–7938 (2014).

30. A. D. Becke, Density-functional thermochemistry. III. The role of exact exchange. *J. Chem. Phys.* **98**, 5648–5652 (1993).

31. J. Tao, J. P. Perdew, V. N. Staroverov, G. E. Scuseria, Climbing the density functional ladder: Nonempirical meta–generalized gradient approximation designed for molecules and solids. *Phys. Rev. Lett.* **91**, 146401 (2003).

32. M. Isegawa, A. K. Sharma, S. Ogo, K. Morokuma, DFT study on Fe(IV)-peroxo formation and H atom transfer triggered O_2 activation by NiFe complex. *Organometallics* **37**, 1534–1545 (2018).

33. M. Isegawa, A. K. Sharma, S. Ogo, K. Morokuma, Electron and hydride transfer in a redox-active NiFe hydride complex: A DFT study. *ACS Catal.* **8**, 10419–10429 (2018).

34. M. Dolg, U. Wedig, H. Stoll, H. Preuss, Ab initio pseudopotential study of the first row transition metal monoxides and iron monohydride. *J. Chem. Phys.* **86**, 2123–2131 (1987).

35. F. Weigend, R. Ahlrichs, Balanced basis sets of split valence, triple zeta valence and quadruple zeta valence quality for H to Rn: Design and assessment of accuracy. *Phys. Chem. Chem. Phys.* **7**, 3297–3305 (2005).

36. A. V. Marenich, C. J. Cramer, D. G. Truhlar, Universal solvation model based on the generalized born approximation with asymmetric descreening. *J. Chem. Theory Comput.* **5**, 2447–2464 (2009).

37. F. Neese, The ORCA program system. *WIREs Comput. Mol. Sci.* **2**, 73–78 (2012).

38. M. Filatov, On the calculation of Mössbauer isomer shift. *J. Chem. Phys.* **127**, 084101 (2007).

39. F. Neese, Prediction and interpretation of the [57]Fe isomer shift in Mössbauer spectra by density functional theory. *Inorg. Chim. Acta* **337**, 181–192 (2002).

40. S. Sinnecker, L. D. Slep, E. Bill, F. Neese, Performance of nonrelativistic and quasi-relativistic hybrid DFT for the prediction of electric and magnetic hyperfine parameters in [57]Fe Mössbauer spectra. *Inorg. Chem.* **44**, 2245–2254 (2005).

41. M. Römelt, S. Ye, F. Neese, Calibration of modern density functional theory methods for the prediction of [57]Fe Mössbauer isomer shifts: Meta-GGA and double-hybrid functionals. *Inorg. Chem.* **48**, 784–785 (2009).

Citation: S. Ogo, T. Kishima, T. Yatabe, K. Miyazawa, R. Yamasaki, T. Matsumoto, T. Ando, M. Kikkawa, M. Isegawa, K.-S. Yoon, S. Hayami, [NiFe], [FeFe], and [Fe] hydrogenase models from isomers. *Sci. Adv.* **6**, eaaz8181 (2020).